Formation and reactivity of a $Mn^{IV}(O)(\mu\text{-}O)Ce^{IV}$ species: A closest mimic of photosystem II

Sikha Gupta,[Ψ] Pragya Arora,[Ψ] Zahra Aghaei,[¥] Baghendra Singh,[Ψ] Timothy A. Jackson,[¥*] Apparao Draksharapu[Ψ*]

[Ψ] Southern Laboratories-208A, Department of Chemistry, Indian Institute of Technology Kanpur, Kanpur-208016, India.

[¥] The University of Kansas, Department of Chemistry and Center for Environmentally Beneficial Catalysis, Lawrence, Kansas 66045, United States.

KEYWORDS: Cerium • High valent Mn-oxo • Photosystem II • Polypyridyl ligands • Redox-active Lewis acid

ABSTRACT: Understanding the basic structure of the oxygen-evolving complex (OEC) in photosystem II (PS-II) and the water oxidation mechanism can aid in the discovery of more efficient and sustainable catalysts for water oxidation. In this context, we present evidence for the formation of a $[(TPA)Mn^{IV}(O)(\mu\text{-}O)Ce^{IV}(NO_3)_3]^+$ (**2**) complex (TPA = tris(pyridyl-2-methyl)amine) by adding aqueous ceric ammonium nitrate to an acetonitrile solution of the $[(TPA)Mn^{II}]^{2+}$ (**1**) complex. This unique intermediate (**2**) was analyzed using various spectroscopic techniques and electrospray ionization mass spectrometry. Remarkably, **2** closely mimics the structure of $Mn^{V}(O)(\mu\text{-}O)Ca^{II}(OH_2)$ observed in the OEC of PS-II. Notably, **2** reacts effectively with ferrocene derivatives, indicating that redox-active Ce^{IV} binding enhances electron transfer efficiency. Additionally, **2** demonstrates the ability to perform oxygen atom transfer and hydrogen atom abstraction reactions. The discovery of this reactive $[(TPA)Mn^{IV}(O)(\mu\text{-}O)Ce^{IV}(NO_3)_3]^+$ adduct provides exciting opportunities for investigating the structure of the $Mn^{V}(O)(\mu\text{-}O)Ca^{II}(OH_2)$ unit in the oxygen-evolving complex.

INTRODUCTION

The oxygen-evolving complex (OEC) in photosystem II (PS-II) facilitates one of the most significant and demanding water-splitting processes.[1-3] The OEC consists of a Mn_4CaO_5 cubane cluster, where three manganese atoms are in the cubane and an additional Mn^{V}-oxo atom is linked to Ca^{2+} via a bridging oxido ligand. This natural architecture incorporates a high-valent Mn^{V}-oxo species as the crucial active intermediate for its function.[2] In recent decades, numerous research groups have endeavored to replicate and understand this complex structure by developing high-valent synthetic metal-oxo compounds using heme and nonheme systems.[3] However, a limited number of spectroscopically characterized nonheme Mn^{V}-oxo species have been observed thus far, including those supported by salen, TAML and $[H_3buea]^{3-}$ ligand frameworks.[4-6] These species have demonstrated chemical reactivities, including C-H bond activation and oxygen atom transfer.[5-9]

Highlighting the ambiguous yet essential role of the calcium ion as a Lewis acid (LA) in the natural OEC, studies have been conducted with various other redox-inactive metal ions such as Mg^{2+}, Zn^{2+}, Lu^{3+}, Y^{3+}, Al^{3+}, and Sc^{3+} on the reported high-valent Mn^{IV}=O intermediates.[10-13] The generated Mn^{IV}=O bound LA species have been observed to alter the Mn^{4+}/Mn^{3+} potential to higher positive values, thereby increasing the reactivity of those species.[11,12] Over the last two decades, significant progress has been made in understanding the mechanisms by which Lewis acids activate high valent metal-oxo species.[10-17] The terminal Mn^{IV}=O's are the most probable sites for outer sphere coordination in LA-bound Mn-oxo species, particularly in pentadentate frameworks like N4Py (N4Py = N,N-bis(2-pyridylmethyl)-N-bis(2-pyridyl)methylamine)), BnTPEN (BnTPEN = N^1-benzyl-N^1,N^2,N^2-tris(pyridine-2-ylmethyl)ethane-1,2-diamine), and DPAQ (DPAQ = 2-[bis(pyridin-2-ylmethyl)]amino-N-quinolin-8-ylacetamide)).[10,14,15]

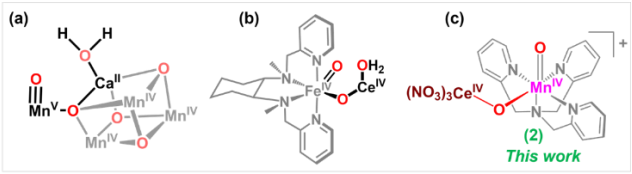

Scheme 1. (a) Structure proposed for the Mn_4CaO_5 cluster in the S_4 state of the OEC in photosystem II.[1,3] Proposed structures of synthetic high valent metal species bearing tetradentate ligand bound to redox-active Ce^{IV}, (b) $[(mcp)Fe^{IV}(O)(\mu\text{-}O)Ce^{IV}(NO_3)_3]^+$,[18] and (c) $[(TPA)Mn^{IV}(O)(\mu\text{-}O)Ce^{IV}(NO_3)_3]^+$ (**2**) (this work).

In contrast, tetradentate frameworks provide an additional coordination site alongside the Mn-oxo site, allowing an incoming LA to bind effectively. Costas and coworkers established the spectroscopic characterization of $[(mcp)Fe^{IV}(O)(\mu\text{-}O)Ce^{IV}(NO_3)_3]^+$ (mcp = N,N'-dimethyl-N,N'-bis(2-pyridylmethyl)-1,2-cis-diaminocyclohexane), which is the closest structural model of the $Mn^{V}(O)(\mu\text{-}O)Ca^{II}$ active

fragment of the OEC in PS-II (Scheme 1).[18] Despite manganese being a key component of PS-II, no studies currently exist on the closest structural mimic of this component, *i.e.*, the presence of terminal Mn=O and Mn-O-LA units in the same molecule. Nam and coworkers reported the first Ce^{IV}-bound Mn-oxo complex, $[(DPAQ)Mn^{IV}=O]^{+}\bullet\bullet\bullet Ce^{IV}$, by reacting $[(DPAQ)Mn^{III}(OH)]^{+}$ with ceric ammonium nitrate (CAN). The $[(DPAQ)Mn^{IV}=O]^{+}\bullet\bullet\bullet Ce^{IV}$ was found to be more reactive than other redox-inactive Lewis acid bound $[(DPAQ)Mn^{IV}=O]^{+}$ complexes.[19] In our recent study, we synthesized and characterized a stable $[(BnTPEN)Mn^{III}–O–Ce^{IV}(NO_3)_4]^{+}$ species.[20] This species is noteworthy as it can serve as a surrogate for several other high-valent Mn intermediates, including $Mn^{IV}–O–Sc^{III}$ and $Mn^{IV}–OH$. The observed equilibrium between two different LA-bound metal-oxo species, $Mn^{III}–O–Ce^{IV}$ and $Mn^{IV}–O–Sc^{III}$, with different stabilities and characteristics in the context of pentadentate ligands, hint at the possible formation of the closest PS-II model with tetradentate ligand framework.

Thus, advancing with the increased complexity of multiple coordination sites in tetradentate neutral ligand design, specifically those with two cis open coordination sites such as TPA (TPA = tris(pyridyl-2-methyl)amine), we explored the possibility of forming a Lewis acid (LA)-bound Mn-oxo species. CAN, which exhibits versatile properties, could act as a redox-active LA and an oxidant in the same mixture.[19,20] Herein, we demonstrate that the reaction of $[(TPA)Mn^{II}(NCMe)(OH_2)](ClO_4)_2$ (**1**) with aqueous CAN generates a unique species $[(TPA)Mn^{IV}(O)(\mu\text{-}O)Ce^{IV}(NO_3)_3]^{+}$ (**2**) in MeCN at 25 °C. This intermediate was characterized using UV-visible absorption, EPR, resonance Raman, X-ray absorption spectroscopy (XAS), X-ray photoelectron spectroscopy (XPS), and electrospray ionization mass spectrometry (ESI-MS). ^{18}O-labelling experiments suggest that both oxygen atoms in the intermediate **2** originate from water. To the best of our knowledge, species **2** is the first reported LA-bound $Mn^{IV}=O$ within a neutral tetradentate framework. More importantly, **2** is the closest structural mimic of $Mn^{V}(O)(\mu\text{-}O)Ca^{II}(OH_2)$ found in the OEC of PS-II. The redox-active Ce(IV) coordination in intermediate **2** makes the Mn center like a *masked* Mn(V) species, similar to PS-II. Reactivity studies, including electron transfer (ET), oxygen atom transfer (OAT), and hydrogen atom abstraction (HAA), were performed with species **2**, revealing notable reactivity trends.

RESULTS AND DISCUSSION

TPA ligand was synthesized by following a previously reported method.[21] Complex **1** was synthesized by mixing an equimolar amount of the ligand TPA and $[Mn^{II}(H_2O)_6](ClO_4)_2$ in MeCN at room temperature.[22] White block-shaped crystals of **1** were obtained by vapor diffusion of ether into this solution. X-ray crystallography revealed that **1** is an octahedral complex (Figure 1), with the N atoms of TPA occupying four coordination sites, while the fifth and sixth cis sites are occupied by water and MeCN. The average $Mn\text{-}N_{py}$ bond distance is 2.244 Å, whereas the $Mn\text{-}N_{amine}$ bond distance is slightly longer, at 2.285 Å, consistent with the Mn(II) oxidation state in the high spin configuration.[23]

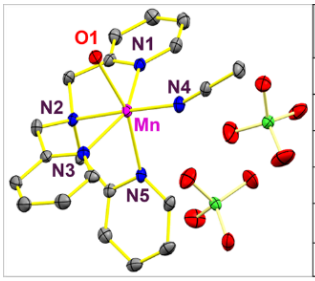

	Bond length (Å)
Mn-N1	2.255(2)
Mn-N2	2.284(2)
Mn-N3	2.218(2)
Mn-N4	2.149(2)
Mn-N5	2.254(2)
Mn-O1	2.185(2)

Figure 1. X-ray crystal structures of **1** with 50% ellipsoid probability level and its bond parameters (left). Hydrogen atoms were omitted for clarity. CCDC 2367364. (right) Selected bond lengths are shown in the table.

To the acetonitrile solution of **1**, 50 µL of H_2O and 4 eq. of CAN were added, resulting in the formation of a green-colored stable species (**2**) with an absorption band at 650 nm ($\varepsilon_{650\ nm}$ = 550 $M^{-1}cm^{-1}$) (Figure 2). Concentration-dependent studies of CAN indicated that 4 eq. of CAN are necessary to produce the maximum yield of **2**. This result, featuring the 650 nm species, initially appears similar to the work by Nam and coworkers reported in 2010. In their study, $[(BQCN)Mn^{II}(OTf)_2]$ reacted with 4 eq. of CAN in acetonitrile:water (9:1, vol/vol) mixture, forming a band at 630 nm ($\varepsilon_{630\ nm}$ = 400 $M^{-1}cm^{-1}$), which was characterized as $[(BQCN)Mn^{IV}=O]^{2+}$.[24]

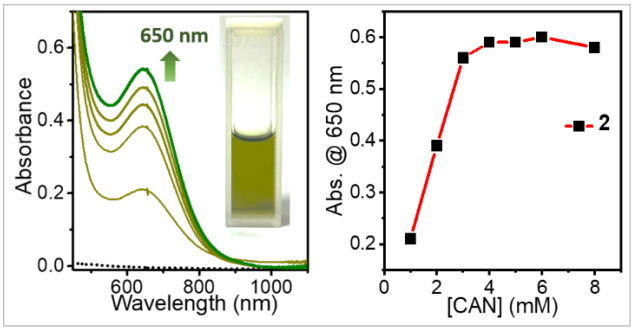

Figure 2. (a) UV-Vis absorption spectral changes depicting the formation of **2** (green) after adding 50 µL H_2O and 4 eq. of CAN to 1 mM **1** (black dotted) in MeCN at 25 °C. (b) Absorbance vs [CAN] plot depicting the formation of 650 nm species in MeCN at 25 °C.

Positive mode electrospray ionization mass spectrometry (ESI-MS) was performed to evaluate the speciation during the reaction of **1** and CAN. The ESI-MS study of **2** shows signals at *m/z* values of 702.94 and 739.90, whose isotopic patterns correspond to $[(TPA)Mn(O)_2Ce(NO_3)_3]^{+}$ and $[(TPA)Mn(O)_2Ce(NO_3)_2(ClO_4)]^{+}$, respectively. Upon using $H_2{}^{18}O$, the signals shifted by four mass units to 706.94 and 743.90, indicating that water is the source of oxygen in species **2** (Figures 3a, S1, and S2). Additionally, another signal was observed at *m/z* = 407.07, corresponding to $[(TPA)Mn^{II}(NO_3)]^{+}$. The oxidation state of **2** was further validated using X-band EPR spectroscopy at 120 K in acetonitrile, which displayed a signal at g = 4.2. This EPR signal indicates the presence of an S = 3/2 species, consistent with the Mn(IV) oxidation state, which has a d^3 configuration

(Figure 3b). Additionally, there is a minor g = 2 signal, exhibiting the characteristic hyperfine splitting of ^{55}Mn, originating from an unidentified Mn(II) species.

Resonance Raman (rR) analysis of **2** was performed using λ_{exc} = 561 nm at room temperature, revealing a resonantly enhanced band at 710 cm^{-1}, which shifted to 685 cm^{-1} upon using $H_2{}^{18}O$. The observed 710 cm^{-1} band closely matches the Mn=O vibration of [(BQCN)Mn^{IV}=O]$^{2+}$ (707 cm^{-1}) reported by Nam and coworkers.[24] Another isotopically sensitive signal appears at 535 cm^{-1}, which shifted to 505 cm^{-1} upon $H_2{}^{18}O$ labelling (Figure 3c). The shift of 25-30 cm^{-1} is consistent with the predicted shift of Mn–O stretch using Hooke's law. The presence of two isotopically sensitive bands at 710 and 535 cm^{-1} in the rR spectrum can be attributed to Mn=O and Mn–O stretches, respectively.

The Mn K-edge XAS near-edge structures of **1** and **2** show a pronounced edge shift from 6549.5 to 6552.8 eV, respectively (Figure 3d), consistent with oxidation of the Mn center. The edge energy of **2** falls within the range observed for Mn^{IV}-oxo, Mn^{IV}-hydroxo, and (μ-oxo)manganese(IV)cerium(IV) complexes (6550 – 6552 eV).[19, 25-31] The pre-edge region of **2** is also perturbed relative to **1** (Figure 3d and S4). The pre-edge spectrum of **1** consists of a peak at 6541.1 eV (area of 3 units) and a shoulder near 6544 eV, while **2** shows two peaks of near equal height at 6541.8 and 6543.5 eV (total area of 16 units). The increase in pre-edge intensity and area for **2** marks a less centrosymmetric environment for the Mn center that gives rise to increased Mn 4p mixing into the 3d manifold. We note, for comparison, that the previously reported (μ-oxo)manganese(IV)cerium(IV) complex had a pre-edge peak intensity similar to that of a Mn^{III}-hydroxo analogue.[19] In a separate XAS study, it was shown that this Mn^{III}-hydroxo complex had a modest peak area of ~5 units, which was essentially the same as that of the corresponding Mn^{II} complex.[32] Thus, it is reasonable to conclude that the previously reported (μ-oxo)manganese(IV)cerium(IV) complex has a modest peak area, potentially less than that of **2**. Collectively, the near-edge properties of **2** lend credence to the Mn^{IV} oxidation state assignment and further show that the geometry is markedly perturbed compared to that of **1**.

The Fourier transform (FT) of EXAFS data for **2** shows prominent peaks at 1.3, 1.7, 2.3, and 3.4 Å (Figure 3e). The large peak at the long distance of 3.4 Å suggests that there is a heavy atom-scatterer a long distance from the Mn center. For comparison, bis(*μ*-oxo)dimanganese(III,IV) complexes typically show a heavy-atom scatterer peak from the Mn•••Mn interaction at an FT EXAFS distance of ~2.3 Å.[33] The FT EXAFS spectrum of **2** resembles that of the (μ-oxo)manganese(IV)cerium(IV) complex of Nam and coworkers, which displayed a similarly intense peak at ~3.3 Å that was fit with a Ce scatterer at 3.67 Å.[19] Our fits of the FT EXAFS data show that the peak at 3.4 Å can be nicely accommodated by a Ce atom ~3.7 Å from the Mn center (Figure 3e and S3, and Table S2). The inner FT EXAFS peaks can be well fit considering an O shell at 1.80 Å, N shells at 2.04 and 2.34 Å and a C shell at 2.91 Å (Table S2). We explored fits that split the two-atom oxygen shell into separate scatterers, but these fits result in Debye-Waller factors less than 0, which is not realistic. Thus, the O scatterer at 1.80 Å and the Ce scatterer at 3.7 Å provide strong support for the presence of a (μ-oxo)manganese(IV)cerium(IV) unit. Although the FT EXAFS data do not provide evidence for a short O distance consistent with a Mn=O unit, it is possible that the data do not allow us to resolve a Mn=O and the O of the (μ-oxo)manganese(IV)cerium(IV) unit. Therefore, the UV-Vis, EPR, XAS, rR, and ESI-MS techniques collectively reveal the existence of the (TPA)Mn^{IV}O(μ-O)Ce^{IV} species in solution, which closely resembles the structure of the oxygen-evolving complex (OEC) in PS-II.

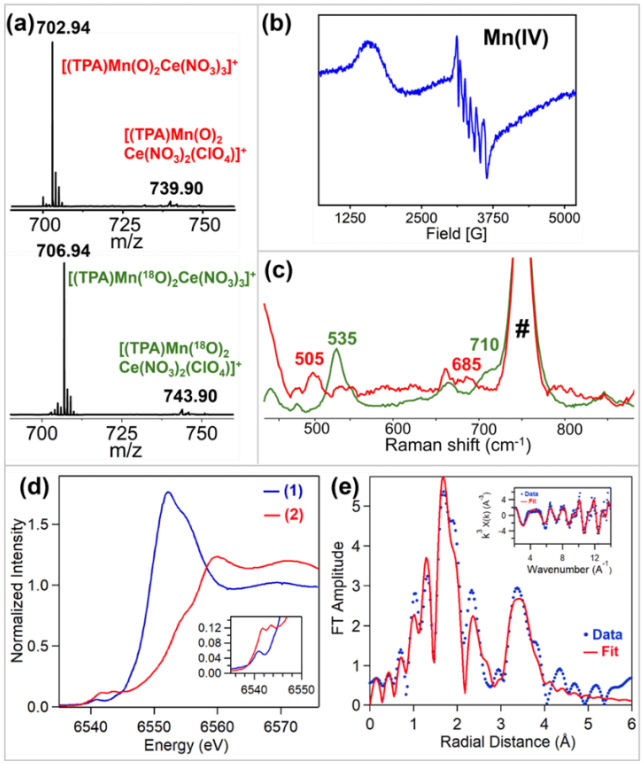

Figure 3. (a) ESI-MS analysis of **2** (top) and **^{18}O-2** (bottom). *Condition to generate* **2**/**^{18}O-2**: **1** + 50 μL $H_2O/H_2{}^{18}O$ + 4 eq. of CAN at 25 ˚C in MeCN. (b) X-band EPR spectrum of **2** at 120 K in MeCN. *Condition to generate* ***2***: 2 mM **1** + 50 μL H_2O + 4 eq. of CAN at 25 ˚C in MeCN. (c) Resonance Raman spectra (λ_{exc} = 561 nm) of **2** (green) and **^{18}O-2** (red) in MeCN at 25 ˚C. # Indicate MeCN peak. *Condition to generate* **2**/**^{18}O-2**: 3 mM **1** + 50 μL $H_2O/H_2{}^{18}O$ + 4 eq. of CAN at 25 ˚C in MeCN. (d) Mn K-edge near-edge spectra of **1** and **2**. Inset: pre-edge features. (e) Fourier transforms of EXAFS data for **2** (blue circles) with a fit (red trace) described in Table S2. The inset shows the raw EXAFS data (blue circles) and fit (red trace).

The prolonged stability of **2** at room temperature allowed us to isolate the intermediate as a solid material. However, all our efforts to crystalize species **2** were unsuccessful thus far. X-ray photoelectron spectroscopy (XPS) was carried out on the isolated solid of **2** and on **1** to determine their elemental compositions. The Mn 2p XPS spectrum of **1** displays two peaks for Mn $2p_{3/2}$ and Mn $2p_{1/2}$ at 641.19 eV and 652.08 eV, (Figure 4a) corresponding to Mn^{II} species.[34] The peak at 645.30 eV is a satellite peak. The N 1s XPS (Figure S5) showed two peaks at 399.10 eV and 399.92 eV attributed to the amine and pyridine N from the ligand.[35] The Mn 2p XPS spectrum of species **2** displays two peaks at binding energies 642.50 eV and 654.23 eV, corresponding to the Mn $2p_{3/2}$ and Mn $2p_{1/2}$, respectively (Figure 4a). The

positive shift of 1.40 eV in binding energy as compared to **1** indicates the higher oxidation state of Mn in **2**. The peaks were well assigned for the Mn^{IV} according to the literature.[34] The Ce 3d XPS was deconvoluted into Ce $3d_{5/2}$ and Ce $3d_{3/2}$ peaks. The peaks at 886.00 eV, 904.44 eV and 917.06 eV were attributed to the Ce^{IV} center (Figure 4b).[36] In addition, two peaks at 882.06 eV and 899.70 eV were observed for the Ce^{III} could be originated from the free Ce(III) component.[36] The peak area ratio of Ce^{IV}/Ce^{III} was determined to be (2.8), suggesting a higher amount of Ce^{IV}. In addition, the N 1s XPS of **2** revealed three peaks at 399.80 eV, 401.86 eV, 406.81 eV assigned for the (pyridine N), (amine N), and (nitrate N) (Figure S6).[35] The O1s XPS also showed three peaks at 532.32 eV, 530.36 eV and 533.73 eV corresponding to the M=O, M-O bonds and N-O (of nitrate), respectively (Figure S6).[37] Altogether, the XPS analyses on the isolated solid of **2** revealed the existence of Mn(IV) and Ce(IV) centers, which is also supported by XAS analysis in solution.

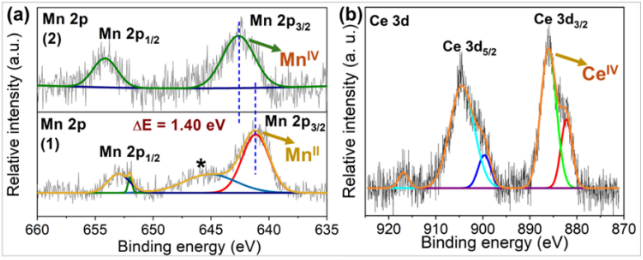

Figure 4. (a) Comparison of Mn 2p XPS spectra of complexes **1** (Mn $2p_{3/2}$ at 641.19 eV and Mn $2p_{1/2}$ at 652.08 eV) and **2** (Mn $2p_{3/2}$ at 642.50 eV and Mn $2p_{1/2}$ at 654.23 eV) showing the positive shift of 1.40 eV in **2** pointing towards higher binding energy suggesting the presence of Mn^{IV}. * Indicates satellite peak. (b) Ce 3d XPS spectrum of **2** (886.00 eV, 904.44 eV and 917.06 eV were attributed to the Ce^{IV}) depicting the presence of Ce^{IV} with higher peak intensity.

Reactivity of 2 in Electron transfer reactions

The electron transfer reactivity of **2** was investigated using various ferrocene derivatives, and the resulting ferrocenium equivalents were determined. After reacting with **2**, ferrocene and acetyl ferrocene produced three oxidizing equivalents of the corresponding ferrocenium, indicating that the potential of **2** is greater than 0.64 V vs. Ag/AgCl (Figure S7). In contrast, diacetyl ferrocene resulted in only 2 oxidizing equivalents of ferrocenium, as it is a weaker reductant. The observation that only 2 equivalents of diacetyl ferrocenium are derived from **2** suggests that the one-electron reduced species of **2** has a potential lower than 0.93 V vs. Ag/AgCl.

Reactivity of 2 in OAT and HAA reactions

The oxygen atom transfer (OAT) reactions and hydrogen atom abstraction (HAA) reactions for **2** were conducted using triphenylphosphine (PPh_3) and trisubstituted phenol derivatives. The reaction rates of **2** with different substrates were measured by analyzing the decay of the 650 nm absorbance band. Pseudo-first-order rate constants (k_{obs}) were calculated by reacting **2** with substrates at various concentrations. The relationship between the rate of reaction (k_{obs}) and the concentration of the substrate ([substrate]) allowed for the estimation of second-order rate constants (k_2). Following reactions with PPh_3, species **2** yielded triphenylphosphine oxide and **1** as organic and inorganic products, respectively, in MeCN at room temperature. To the resultant solution, the addition of 4 eq. of CAN regenerates intermediate **2** (Figure S13). The experimental k_2 value for PPh_3 is 1.3 $M^{-1}s^{-1}$ (Figure S8). Additionally, **2** reacts with thioanisole; however, our attempt to obtain k_2 for thioanisole was unsuccessful due to precipitate formation in the reaction mixture.

In addition, **2** displays significant HAA reactivity towards trisubstituted phenols such as 4-X-2,6-di-tert-butylphenol (4-X-2,6-DTBP) (X = H, OMe, ^{t}Bu, and Me). The observed k_2 values are 70 $M^{-1}s^{-1}$ for 4-OMe-2,6-di-tert-butylphenol, 0.1 $M^{-1}s^{-1}$ for 4-Me-2,6-di-tert-butylphenol, 1.5 × 10^{-2} $M^{-1}s^{-1}$ for 4-^{t}Bu-2,6-di-tert-butylphenol, and 1 × 10^{-2} $M^{-1}s^{-1}$ for 2,6-di-tert-butylphenol (Figure S9). These observed k_2 values decrease with increases in the phenols' O–H bond dissociation energy (BDE). A linear relationship is evident when plotting the log(k_2) against the BDE of the O–H bond, indicating that as the BDE decreases, the reaction rate increases (Figure 5a). Also, the faster rates obtained using different electron-donating substituents results in a negative slope of ρ = -5. 2 in the Hammet analysis, indicate the electrophilic character of **2** (Figure 5b).

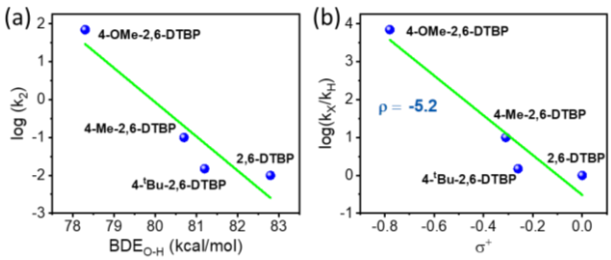

Figure 5. (a) The plot of BDE_{O-H} vs. log k_2 and (b) Hammett correlation for the reaction of **2** with para-X-substituted phenol derivatives at 25 °C.

Literature reports suggest that the oxidation of phenols using high-valent metal species typically results in the formation of phenoxyl radicals. These radicals then undergo further radical coupling reactions to form dimerized products.[38,39] Product analysis was conducted using ESI-MS spectrometry, which suggests the formation of a dimerized product DPQ (~30%) in the case of 2,6-di-tert-butylphenol (Figure S10). However, in the case of 4-OMe-2,6-DTBP and 4-^{t}Bu-2,6-DTBP the corresponding UV–vis absorption spectra revealed the formation of phenoxyl radical (71% of 4-MeO-2,6-DTBP$^•$, and 94% of 2,4,6-TTBP$^•$) that gradually formed 2,6-di-*tert*-butyl-1,4-benzoquinone (BQ) as the product (Figure S11, S14). For 4-Me-2,6-DTBP the 2,6-di-tert-butyl-4-methylene-2,5-cyclohexadienone product was identified from ESI-MS studies (Figure S14g).

To put our studies into a broader context, we employed 4-CN-phenol, a substrate with a strong O-H bond (BDE_{O-H} = 93.1 kcal/mol), to compare reactivity with high-valent manganese intermediates, namely (BnTPEN)Mn(III)-O-Ce(IV) and $[(BQCN)Mn^{IV}=O]^{2+}$, both of which were generated with CAN, These reactions indicate that intermediate **2** exhibits

a comparable rate constant (k_2 of 0.028 M^{-1} s^{-1} at 25 °C) to that of the (BnTPEN)Mn(III)-O-Ce(IV) species (k_2 of 0.027 M^{-1} s^{-1} at 25 °C) (Figure S12). However, due to precipitate formation, we could not measure the k_2 value for the reaction between $[(BQCN)Mn^{IV}=O]^{2+}$ and 4-CN-phenol. Alternatively, we successfully measured the k_2 values for the reactivity of 2,6-DTBP with these intermediates. Notably, **2** (k_2 of 0.01 M^{-1} s^{-1} at 25 °C) demonstrated a 7-fold and 60-fold reduction in k_2 when compared to the (BnTPEN)Mn(III)-O-Ce(IV) (k_2 of 0.073 M^{-1} s^{-1} at 25 °C) and $[(BQCN)Mn^{IV}=O]^{2+}$ (k_2 of 0.672 M^{-1} s^{-1} at 25 °C) species, respectively (Figure S12). The relatively lower reactivity rates of **2** and (BnTPEN)Mn(III)-O-Ce(IV) compared to $[(BQCN)Mn^{IV}=O]^{2+}$ imply that steric hindrance from the bulkier bound Lewis acid (cerium) adjacent to the active site is impacting the reactivity. The modest reactivity of **2** can also be attributed to the presence of two anionic ligands (the terminal and bridging oxo groups), which would tend to suppress the oxidizing power of the Mn^{IV} center. In this sense, **2** bears resemblance to the oxohydroxomanganese(IV) complexes of Busch[40] and Costas, which showed low reactivity compared to oxomanganese(IV) complexes with neutral pentadentate ligands.

Electrocatalytic water oxidation

We evaluated the water oxidation activity of **1** by immobilizing it onto nickel foam (NF) using a Nafion binder to create the **1@NF** electrode. This electrode was tested for electrocatalytic water oxidation in a 1.0 M KOH solution. The results showed that **1** exhibited excellent activity, achieving a current density of 10 mA/cm^2 at an overpotential of 360 mV (Figure 6). For comparison, we evaluated the water oxidation performance of $Mn(II)Cl_2$ salt on nickel foam using the same procedure, and it demonstrated poor activity. The electrocatalytic water oxidation performance of **1** surpassed that of previously reported Mn-based complexes.[42-47] For instance, $[Mn^{II}(H_2O)_2(X)_2(dcbpy)]$ immobilized on a gold electrode achieved a current density of 1.6 mA cm^{-2} at an overpotential of 310 mV.[42] Similarly, MnL_2 (where HL = (E)-3-hydroxy-N'-(pyridin-2-ylmethylene)-2-naphthohydrazide) on a carbon paste electrode (CPE) exhibited an overpotential of 565 mV to reach a current density of 10 mA cm^{-2}.[43] Mn^{II}-salophen complexes immobilized on CPE achieved the same current density with overpotentials between 345 and 420 mV.[44] Beyond Mn-based complexes, Ni and Sb corrole complexes immobilized on nickel foam displayed overpotentials of 330 mV and 360 mV, respectively, for 10 and 50 mA cm^{-2} current densities.[45,46] Additionally, ruthenium azobis(benzothiazole) complexes on carbon cloth reached 10 mA cm^{-2} with overpotentials ranging from 326 to 370 mV.[47] Among the reported systems, **1** demonstrated an efficient catalytic performance.

To further investigate the water oxidation process, chronoamperometric testing was conducted, revealing the production of approximately 0.27 mmol of O_2 after 30 minutes (Figure 6). Additionally, headspace Raman spectroscopy detected a vibrational band at 1556 cm^{-1} (Figure S15), which corresponds to the O=O stretching mode of dioxygen generated during the water oxidation process. These data indicate the promising potential of complex **1** for applications in electrocatalytic water oxidation reactions.

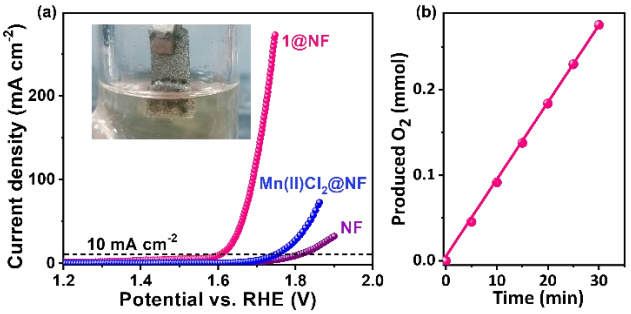

Figure 6. (a) Water oxidation activity of **1** compared with $Mn(II)Cl_2$ in alkaline medium. Inset: A digital photograph showing the oxygen production from **1@NF**. (b) Plot for the produced oxygen under chronoamperometric testing.

CONCLUSION

Over the past few years, numerous PS-II model complexes have been synthesized in attempts to replicate its function in water oxidation. A particularly successful result was reported for an iron-based oxygen-evolving complex, $[(mcp)Fe^{IV}(O)(\mu\text{-}O)Ce^{IV}(NO_3)_3]^+$. However, the present study is unique in its utilization of manganese to develop a model complex that closely resembles the structure of the OEC in PS-II, given that Mn is the primary constituent of PS-II. This study investigates the generation of $[(TPA)Mn^{IV}(O)(\mu\text{-}O)Ce^{IV}(NO_3)_3]^+$ (**2**) by introducing aqueous CAN to an acetonitrile solution of the $[(TPA)Mn^{II}]^{2+}$ complex, which employs a tetradentate ligand with two cis coordination sites. This unique intermediate **2** was thoroughly analyzed using UV-visible spectroscopy, EPR, XPS, XAS, rR, and ESI-MS. Complex **2** is an even closer structural mimic of the active site fragment of PS-II, *i.e.*, $Mn^{V}(O)(\mu\text{-}O)Ca^{II}(OH_2)$. Notably, **2** reacts with Fc and AcFc, yielding 3 equivalents of the corresponding ferrocenium ions, suggesting that **1** gained three oxidizing equivalents upon its reaction with CAN. Additionally, complex **1** demonstrated promising electrocatalytic water oxidation activity, achieving a current density of 10 mA/cm^2 at an overpotential of 360 mV. Furthermore, **2** demonstrates the capability to perform oxygen atom transfer and hydrogen atom abstraction reactions. Complex **2** holds the potential to afford a deeper understanding of the role of Lewis acid, which could contribute significantly to the advancement of artificial photosynthetic systems.

EXPERIMENTAL DETAILS

Synthesis of Complex 1

The synthesis of the ligand was conducted following a literature method.[21] To a 2 mL acetonitrile solution of the TPA ligand (0.45 mmol), an equimolar amount of $[Mn^{II}(H_2O)_6](ClO_4)_2$ was added, and the mixture was stirred for 4 hours. Subsequently, half of the solvent was evaporated using a rotary evaporator. A white precipitate formed upon the addition of diethyl ether. The precipitate was then washed with diethyl ether and dried under reduced pressure. White block-shaped crystals suitable for X-ray crystallographic analysis were obtained by allowing diethyl ether to diffuse into the acetonitrile solution of **1** over two days.

Sample preparation for EPR experiments

To generate 650 nm species, 2 mM **1** was treated with 4 eq. CAN and 50 µL water, generated **2** in acetonitrile. The mixture was subsequently frozen in liquid nitrogen, and EPR measurements were taken at 120 K.

Sample preparation for resonance Raman experiments

To generate 650 nm species, 3 mM **1** was treated with 4 eq. CAN and 50 µL water in acetonitrile and resonance Raman spectrum was recorded at 25 ^{o}C with 561 nm excitation wavelength. For ^{18}O labelling experiment, 50 µL $H_2{}^{18}O$ was used instead.

Sample preparation for ESI-MS experiments

Positive mode ESI-MS data was recorded using 1 mM **1** with 4 eq. CAN and 50 µL water in acetonitrile at room temperature. For ^{18}O labelling experiment, 50 µL $H_2{}^{18}O$ was used instead.

Sample preparation for XAS experiments

To make an XAS sample for **2**, a stock solution of 200 mM ceric ammonium nitrate (CAN) was prepared in acetonitrile at room temperature. The solution was sonicated for approximately 10 minutes, until transparent. 20 µL of distilled water and 198 µL of the CAN stock solution were added, respectively, to a 5.5 mM solution of **1** in 1.8 ml CH_3CN. After filtering this solution with a PTFE filter (0.45 µm), roughly 0.5 mL of the filtered solution was immediately transferred to an XAS cup and frozen in liquid nitrogen. The UV-Vis spectra collected for the same stock solution showed the formation of **2**. The XAS sample of complex **1** was made by preparing a 10 mM solution of **1** in 2 ml acetonitrile and transferring roughly 0.5 mL of this solution to an XAS cup that was flash frozen in liquid nitrogen. Before collecting XAS data, both samples were stored in liquid nitrogen.

Sample preparation for XPS analysis

For XPS analysis, a solid sample of **2** was isolated. In a concentrated solution of **2** (15 mM), the addition of diethyl ether led to the formation of a green precipitate. This precipitate was washed with diethyl ether, dried and subsequently isolated as a green solid for XPS analysis.

Preparation of **1@NF** and **Mn(II)Cl_2@NF** electrodes

A solution of compound **1** (5 mg) was prepared by dissolving it in 50 µL of acetonitrile, followed by the addition of 10 µL of a 0.05 wt% Nafion solution in ethanol. The mixture was subjected to sonication for 5 minutes and subsequently applied onto nickel foam (NF) via drop-casting. After deposition, the **1@NF** composite was dried at 50 °C for 6 hours. Its performance in water oxidation was then evaluated. A similar procedure was employed for the preparation of **Mn(II)Cl_2@NF**, substituting 5 mg of Mn(II)Cl_2 salt in place of **1**.

ASSOCIATED CONTENT

Supporting Information. Experimental details, synthesis of **1**, characterization of **2**, ferrocene reactivity, product analyses and other spectroscopic data. This material is available free of charge via the Internet at http://pubs.acs.org.

CCDC 2367364 contains the supplementary crystallographic data for this paper. These data can be obtained free of charge via www.ccdc.cam.ac.uk/data_request/cif, by emailing data_request@ccdc.cam.ac.uk, or by contacting The Cambridge Crystallographic Data Centre, 12 Union Road, Cambridge CB2 1EZ, UK.

AUTHOR INFORMATION

Corresponding Authors

Apparao Draksharapu - Southern Laboratories-208A, Department of Chemistry, Indian Institute of Technology Kanpur, Kanpur-208016, India. E-mail: *appud@iitk.ac.in*

Timothy A. Jackson – The University of Kansas, Department of Chemistry and Center for Environmentally Beneficial Catalysis, Lawrence, Kansas 66045, United States; orcid.org/0000-0002-3529-2715; Email: *taj@ku.edu*

Authors

Sikha Gupta - Southern Laboratories-208A, Department of Chemistry, Indian Institute of Technology Kanpur, Kanpur-208016, India.

Pragya Arora - Southern Laboratories-208A, Department of Chemistry, Indian Institute of Technology Kanpur, Kanpur-208016, India.

Zahra Aghaei – The University of Kansas, Department of Chemistry and Center for Environmentally Beneficial Catalysis, Lawrence, Kansas 66045, United States.

Baghendra Singh - Southern Laboratories-208A, Department of Chemistry, Indian Institute of Technology Kanpur, Kanpur-208016, India.

Author Contributions

The manuscript was written through contributions of all authors. All authors have given approval to the final version of the manuscript.

Funding Sources

The research reported in this work is financially supported by SERB (CRG/2023/001112), CSIR (01(3050)/21/EMR-II) and NSF (CHE-2154955).

Notes

The authors declare no competing financial interest.

ACKNOWLEDGMENT

The research reported in this work is financially supported by SERB (CRG/2023/001112) & CSIR (01(3050)/21/EMR-II) to A.D., and NSF CHE-2154955 (to T.A.J.). We thank the Department of Chemistry, IIT Kanpur, for the analytical facilities. We thank Mr. Subhankar Pradhan for the assistance in the synthesis of BQCN ligand. S.G. and P.A. are thankful to CSIR PhD fellowship and Prime Minister's Research Fellowship, respectively.

REFERENCES

(1) Yano, J.; Yachandra, V. Mn_4Ca Cluster in Photosynthesis: Where and How Water Is Oxidized to Dioxygen. *Chem. Rev.* **2014**, *114* (8), 4175–4205.

(2) Umena, Y.; Kawakami, K.; Shen, J. R.; Kamiya, N. Crystal Structure of Oxygen-Evolving Photosystem II at a Resolution of 1.9 Å. *Nature* **2011**, *473* (7345), 55–60.

(3) Guo, M.; Corona, T.; Ray, K.; Nam, W. Heme and Nonheme High-Valent Iron and Manganese Oxo Cores in Biological and Abiological Oxidation Reactions. *ACS Cent. Sci.* **2019**, *5* (1), 13–28.

(4) Bryliakov, K. P.; Talsi, E. P. Active Sites and Mechanisms of Bioinspired Oxidation with H_2O_2, Catalyzed by Non-Heme Fe and Related Mn Complexes. *Coord. Chem. Rev.* **2014**, *276*, 73–96.

(5) Taguchi, T.; Gupta, R.; Lassalle-Kaiser, B.; Boyce, D. W.; Yachandra, V. K.; Tolman, W. B.; Yano, J.; Hendrich, M. P.; Borovik, A. S. Preparation and Properties of a Monomeric High-Spin Mn^{V}-Oxo Complex. *J. Am. Chem. Soc.* **2012**, *134* (4), 1996–1999.

(6) Hong, S.; Lee, Y. M.; Sankaralingam, M.; Vardhaman, A. K.; Park, Y. J.; Cho, K. Bin; Ogura, T.; Sarangi, R.; Fukuzumi, S.; Nam, W. A Manganese(V)-Oxo Complex: Synthesis by Dioxygen Activation and Enhancement of Its Oxidizing Power by Binding Scandium Ion. *J. Am. Chem. Soc.* **2016**, *138* (27), 8523–8532.

(7) Arora, P.; Gupta, S.; Kumari Vechalapu, S.; Kumar, R.; Awasthi, A.; Senthil, S.; Khanna, S.; Allimuthu, D.; Draksharapu, A. Mn(II) Polypyridyl Complexes: Precursors to High Valent Mn(V)=O Species and Inhibitors of Cancer Cell Proliferation. *Chem. - A Eur. J.* **2023**, *29*, e202301506.

(8) Arora, P.; Kumari Vechalapu, S.; Duraisamy, S.; Allimuthu, D.; Draksharapu, A. Pivotal Role of Salicylates in Tuning the Formation and Reactivity of Mn(V)=O's. *Eur. J. Inorg. Chem.* **2024**, *27*, e202400079.

(9) Gupta, S.; Sharma, P.; Jain, K.; Chandra, B.; Mallojjala, S. C.; Draksharapu, A. Proton-Assisted Activation of a Mn^{III}-OOH for Aromatic C-H Hydroxylation through a Putative [Mn^{V}=O] Species. *Chem. Commun.* **2024**, *60*, 6520–6523.

(10) Sankaralingam, M.; Lee, Y. M.; Pineda-Galvan, Y.; Karmalkar, D. G.; Seo, M. S.; Jeon, S. H.; Pushkar, Y.; Fukuzumi, S.; Nam, W. Redox Reactivity of a Mononuclear Manganese-Oxo Complex Binding Calcium Ion and Other Redox-Inactive Metal Ions. *J. Am. Chem. Soc.* **2019**, *141* (3), 1324–1336.

(11) Fukuzumi, S.; Ohkubo, K.; Lee, Y. M.; Nam, W. Lewis Acid Coupled Electron Transfer of Metal-Oxygen Intermediates. *Chem. - A Eur. J.* **2015**, *21* (49), 17548–17559.

(12) Liu, Y.; Lau, T. C. Activation of Metal Oxo and Nitrido Complexes by Lewis Acids. *J. Am. Chem. Soc.* **2019**, *141* (9), 3755–3766.

(13) Devi, T.; Lee, Y. M.; Nam, W.; Fukuzumi, S. Metal Ion-Coupled Electron-Transfer Reactions of Metal-Oxygen Complexes. *Coord. Chem. Rev.* **2020**, *410*, 213219.

(14) Chen, J.; Lee, Y. M.; Davis, K. M.; Wu, X.; Seo, M. S.; Cho, K. Bin; Yoon, H.; Park, Y. J.; Fukuzumi, S.; Pushkar, Y. N.; Nam, W. A Mononuclear Non-Heme Manganese(IV)-Oxo Complex Binding Redox-Inactive Metal Ions. *J. Am. Chem. Soc.* **2013**, 135, 6388–6391.

(15) Yoon, H.; Lee, Y. M.; Wu, X.; Cho, K. Bin; Sarangi, R.; Nam, W.; Fukuzumi, S. Enhanced Electron-Transfer Reactivity of Nonheme Manganese(IV)-Oxo Complexes by Binding Scandium Ions. *J. Am. Chem. Soc.* **2013**, *135* (24), 9186–9194.

(16) Gupta, G.; Bera, M.; Paul, S.; Paria, S. Electrochemical Properties and Reactivity Study of [Mn^{V}(O)(μ-OR-Lewis Acid)] Cores. *Inorg. Chem.* **2021**, *60* (23), 18006–18016.

(17) Fukuzumi, S.; Morimoto, Y.; Kotani, H.; Naumov, P.; Lee, Y. M.; Nam, W. Crystal Structure of a Metal Ion-Bound Oxoiron(IV) Complex and Implications for Biological Electron Transfer. *Nat. Chem.* **2010**, *2* (9), 756–759.

(18) Codolà, Z.; Gómez, L.; Kleespies, S. T.; Que, L.; Costas, M.; Lloret-Fillol, J. Evidence for an Oxygen Evolving Iron-Oxo-Cerium Intermediate in Iron-Catalysed Water Oxidation. *Nat. Commun.* **2015**, *6*, 5865

(19) Karmalkar, D. G.; Sankaralingam, M.; Seo, M. S.; Ezhov, R.; Lee, Y. M.; Pushkar, Y. N.; Kim, W. S.; Fukuzumi, S.; Nam, W. A High-Valent Manganese(IV)–Oxo–Cerium(IV) Complex and Its Enhanced Oxidizing Reactivity. *Angew. Chemie - Int. Ed.* **2019**, *58* (45), 16124–16129.

(20) Gupta, S.; Arora, P.; Kumar, R.; Awasthi, A.; Chandra, B.; Eerlapally, R.; Xiong, J.; Guo, Y.; Que, L.; Draksharapu, A. Formation of a Reactive [Mn(III)–O–Ce(IV)] Species and Its Facile Equilibrium with Related Mn(IV)(OX) (X = Sc or H) Complexes. *Angew. Chemie - Int. Ed.* **2024**, 63, e202316378.

(21) Vechalapu, S. K.; Kumar, R.; Chatterjee, N.; Gupta, S.; Khanna, S.; Thimmappa, P. Y.; Senthil, S.; Eerlapally, R.; Joshi, M. B.; Misra, S. K.; Draksharapu, A.; Allimuthu, D. Redox Modulator Iron Complexes Trigger Intrinsic Apoptosis Pathway in Cancer Cells. *iScience* **2024**, *27* (6), 109899.

(22) Aratani, Y.; Yamada, Y.; Fukuzumi, S. Selective Hydroxylation of Benzene Derivatives and Alkanes with Hydrogen Peroxide Catalysed by a Manganese Complex Incorporated into Mesoporous Silica-Alumina. *Chem. Commun.* **2015**, *51*, 4662–4665.

(23) Ward, A. L.; Elbaz, L.; Kerr, J. B.; Arnold, J. Nonprecious Metal Catalysts for Fuel Cell Applications: Electrochemical Dioxygen Activation by a Series of First Row Transition Metal Tris(2-Pyridylmethyl)Amine Complexes. *Inorg. Chem.* **2012**, *5*,4694–4706.

(24) Sawant, S. C.; Wu, X.; Cho, J.; Cho, K. Bin; Kim, S. H.; Seo, M. S.; Lee, Y. M.; Kubo, M.; Ogura, T.; Shaik, S.; Nam, W. Water as an Oxygen Source: Synthesis, Characterization, and Reactivity Studies of a Mononuclear Nonheme Manganese(IV) Oxo Complex. *Angew. Chemie - Int. Ed.* **2010**, *49* (44), 8190–8194.

(25) Massie, A. A.; Denler, M. C.; Singh, R.; Sinha, A.; Nordlander, E.; Jackson, T. A. Structural Characterization of a Series of N5-Ligated Mn^{IV}-Oxo Species. *Chem. - A Eur. J.* **2020**, *26*, 900–912. (25) Massie, A. A.; Denler, M. C.; Singh, R.; Sinha, A.; Nordlander, E.; Jackson, T. A. Structural Characterization of a Series of N5-Ligated MnIV-Oxo Species. *Chem. - A Eur. J.* **2020**, *26*, 900–912.

(26) Singh, P.; Lee, Y.; Mayfield, J. R.; Singh, R.; Denler, M. C.; Jones, S. D.; Day, V. W.; Nordlander, E.; Jackson, T. A., Enhanced Understanding of Structure–Function Relationships for Oxomanganese(IV) Complexes. *Inorg. Chem.* **2023,** *62* (45), 18357-18374.

(27) Leto, D. F.; Jackson, T. A., Mn K-Edge X-ray Absorption Studies of Oxo- and Hydroxo-manganese(IV) Complexes: Experimental and Theoretical Insights into Pre-Edge Properties. *Inorg. Chem.* **2014,** *53* (12), 6179-6194.

(28) Leto, D. F.; Ingram, R.; Day, V. W.; Jackson, T. A., Spectroscopic properties and reactivity of a mononuclear oxomanganese(iv) complex. *Chem. Commun.* **2013,** *49* (47), 5378-5380.

(29) Kurahashi, T.; Kikuchi, A.; Shiro, Y.; Hada, M.; Fujii, H., Unique Properties and Reactivity of High-Valent Manganese–Oxo versus Manganese–Hydroxo in the Salen Platform. *Inorg. Chem.* **2010,** *49* (14), 6664-6672.

(30) Ayougou, K.; Bill, E.; Charnock, J. M.; Garner, C. D.; Mandon, D.; Trautwein, A. X.; Weiss, R.; Winkler, H., Characterization of an Oxo(porphyrinato)manganese(IV) Complex by X-ray Absorption Spectroscopy. *Angew. Chem. Int. Ed. Engl.* **1995,** *34* (3), 343-346.

(31) Gupta, R.; Taguchi, T.; Lassalle-Kaiser, B.; Bominaar, E. L.; Yano, J.; Hendrich, M. P.; Borovik, A. S., High-spin Mn–oxo complexes and their relevance to the oxygen-evolving complex within photosystem II. *Proc. Natl. Acad. Sci. U.S.A.* **2015,** *112* (17), 5319-5324.

(32) Rice, D. B.; Wijeratne, G. B.; Jackson, T. A. Mn K-Edge X-Ray Absorption Studies of Mononuclear Mn(III)–Hydroxo Complexes. *J. Biol. Inorg. Chem.* **2017**, *22*, 1281–1293.

(33) Leto, D. F.; Chattopadhyay, S.; Day, V. W.; Jackson, T. A. Reaction Landscape of a Pentadentate N5-Ligated Mn^{II} Complex with O_2– and H_2O_2 Includes Conversion of a Peroxomanganese(III) Adduct to a Bis(μ-Oxo)Dimanganese(III, IV) Species. *J. Chem. Soc. Dalt. Trans.* **2013**, *42* (36), 13014–1302.

(34) Nesbitt, H. W.; Banerjee, D. Interpretation of XPS Mn(2p) spectra of Mn oxyhydroxides and constraints on the mechanism of MnO_2 precipitation No Title. *Am. Mineral.* **1998**, *83* (3–4), 305–315.

(35) Murphy, E.; Liu, Y.; Matanovic, I.; Rüscher, M.; Huang, Y.; Ly, A.; Guo, S.; Zang, W.; Yan, X.; Martini, A.; Timoshenko, J.; Cuenya, B. R.; Zenyuk, I. V.; Pan, X.; Spoerke, E. D.; Atanassov, P. Elucidating

Electrochemical Nitrate and Nitrite Reduction over Atomically-Dispersed Transition Metal Sites. *Nat. Commun.* **2023**, *14* (1), 4–6.

(36) Chen, J.; Shen, S.; Wu, P.; Guo, L. Nitrogen-Doped CeOx Nanoparticles Modified Graphitic Carbon Nitride for Enhanced Photocatalytic Hydrogen Production. *Green Chem.* **2015**, *17* (1), 509–517.

(37) Frankcombe, T. J.; Liu, Y. Interpretation of Oxygen 1s X-Ray Photoelectron Spectroscopy of ZnO. *Chem. Mater.* **2023**, *35* (14), 5468–5474.

(38) Wu, T.; MacMillan, S. N.; Rajabimoghadam, K.; Siegler, M. A.; Lancaster, K. M.; Garcia-Bosch, I. Structure, Spectroscopy, and Reactivity of a Mononuclear Copper Hydroxide Complex in Three Molecular Oxidation States. *J. Am. Chem. Soc.* **2020**, *142* (28), 12265– 12276.

(39) Unjaroen, D.; Gericke, R.; Lovisari, M.; Nelis, D.; Mondal, P.; Pirovano, P.; Twamley, B.; Farquhar, E. R.; McDonald, A. R. High-Valent d(7) Ni(III) versus d(8) Cu(III) Oxidants in PCET. *Inorg. Chem.* **2019**, *58*, 16838– 16848.

(40) Yin, G.; Danby, A. M.; Kitko, D.; Carter, J. D.; Scheper, W. M.; Busch, D. H., Oxidative Reactivity Difference among the Metal Oxo and Metal Hydroxo Moieties: pH Dependent Hydrogen Abstraction by a Manganese(IV) Complex Having Two Hydroxide Ligands. *J. Am. Chem. Soc.* **2008,** *130* (48), 16245-16253.

(41) Garcia-Bosch, I.; Company, A.; Cady, C. W.; Styring, S.; Browne, W. R.; Ribas, X.; Costas, M., Evidence for a Precursor Complex in C-H Hydrogen Atom Transfer Reactions Mediated by a Manganese(IV) Oxo Complex. *Angew. Chem. Int. Ed.* **2011,** *50* (25), 5648-5653.

(42) Mahanta, A.; Barman, K.; Jasimuddin, S. K. Electrocatalytic Water Oxidation with Surface Anchored Mononuclear Manganese (II) - Polypyridine Complexes. *Chemistry Select* **2019**, *4*, 11740–11747.

(43) Shaghaghi, Z.; Bikas, R.; Heshmati-Sharabiani, Y.; Trzybiński, D.; Woźniak, K. Investigation of electrocatalytic activity of a new mononuclear Mn(II) complex for water oxidation in alkaline media. *Photosynth Res* **2022**, *154*, 369–381.

(44) Shaghaghi, Z.; Mohammad-Rezaei, R.; Jafari, S. Efficient electrochemical water oxidation mediated by different substituted manganese-salophen complexes. *J. Electroanal. Chem.* **2022**, *922*, 116733.

(45) Nayak, P.; Singh, A. K.; Nayak, M.; Kar, S.; Sahu, K.; Meena, K.; Topwal, D.; Indra, A.; Kar, S. Structural modification of nickel tetra(thiocyano)corroles during electrochemical water oxidation. *Dalton Trans.* **2024**, ***53***, 14922-14932.

(46) Pain, T.; Singh, A. K.; Tarai, A.; Mondal, S.; Indra, A.; Kar, S. C–H Bond Activation by an Antimony(V) Oxo Intermediate Accessed through Electrochemical Oxidation of Antimony(III) Tetrakis(thiocyano)corrole. *Inorg. Chem.* **2023**, *62*, 18779–18788.

(47) Singh, A.; Singh, B.; Dey, S.; Indra, A.; Lahiri, G. K. Ruthenium Azobis(benzothiazole): Electronic Structure and Impact of Substituents on the Electrocatalytic Single-Site Water Oxidation Process. *Inorg. Chem.* **2023**, *62*, 2769–2783.

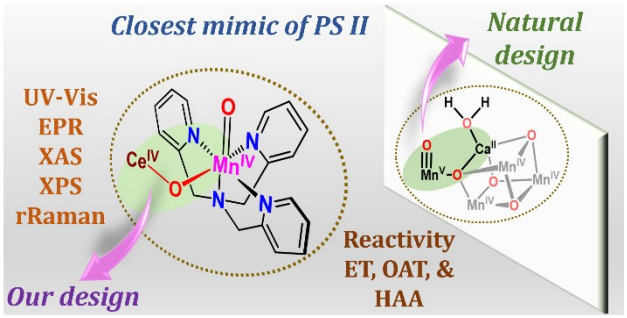
Closest mimic of PS II
Natural design
UV-Vis
EPR
XAS
XPS
rRaman
Reactivity
ET, OAT, &
HAA
Our design